


Article

Effect of Bimetallic Dimer-Embedded $\text{TiO}_2(101)$ Surface on CO_2 Reduction: The First-Principles Calculation

Chongyang Li ^{1,2} , Cui Shang ³, Bin Zhao ^{4,*}, Gang Zhang ¹, Liangliang Liu ^{5,*}, Wentao Yang ⁴ and Zhiquan Chen ^{2,*}

¹ College of Electric Power, North China University of Water Resources and Electric Power, Zhengzhou 450045, China; lichongyang@ncwu.edu.cn (C.L.); zg15937100954@163.com (G.Z.)

² Hubei Nuclear Solid Physics Key Laboratory, Department of Physics, Wuhan University, Wuhan 430072, China

³ Henan Key Laboratory of Magneto-electronic Information Functional Materials, School of Physics and Electronics Engineering, Zhengzhou University of Light Industry, Zhengzhou 450002, China; sc0906@zzuli.edu.cn

⁴ School of Science, Zhongyuan University of Technology, Zhengzhou 450007, China; zhouko2008@163.com

⁵ Key Laboratory for Special Functional Materials of Ministry of Education, Henan University, Kaifeng 475004, China

* Correspondence: zhaobin@zut.edu.cn (B.Z.); liull@henu.edu.cn (L.L.); chenzq@whu.edu.cn (Z.C.)

Abstract: The first-principles calculation was used to explore the effect of a bimetallic dimer-embedded anatase $\text{TiO}_2(101)$ surface on CO_2 reduction behaviors. For the dimer-embedded anatase $\text{TiO}_2(101)$ surface, Zn-Cu, Zn-Pt, and Zn-Pd dimer interstitials could stably stay on the $\text{TiO}_2(101)$ surface with a binding energy of about -2.36 eV, as well as the electronic states' results. Meanwhile, the results of adsorption energy, structure parameters, and electronic states indicated that CO_2 was first physically and then chemically adsorbed much more stably on these three kinds of dimer-embedded $\text{TiO}_2(101)$ substrate with a small barrier energy of 0.03 eV, 0.23 eV, and 0.12 eV. Regarding the reduction process, the highest-energy barriers of the CO_2 molecule on the Zn-Cu dimer-embedded $\text{TiO}_2(101)$ substrate was 0.31 eV, which largely benefited the CO_2 -reduction reaction (CO_2RR) activity and was much lower than that of the other two kinds of Zn-Pt and Cu-Pt dimer- TiO_2 systems. Simultaneously, the products CO^* and $^*\text{O}^*$ of CO_2 reduction were firmly adsorbed on the dimer-embedded $\text{TiO}_2(101)$ surface. Our results indicated that a non-noble Zn-Cu dimer might be a more suitable and economical choice, which might theoretically promote the designation of high CO_2RR performance on TiO_2 catalysts.

Keywords: dimer; $\text{TiO}_2(101)$; CO_2 reduction; metal-embedded; catalyst; first principles



Citation: Li, C.; Shang, C.; Zhao, B.; Zhang, G.; Liu, L.; Yang, W.; Chen, Z. Effect of Bimetallic Dimer-Embedded $\text{TiO}_2(101)$ Surface on CO_2 Reduction: The First-Principles Calculation. *Materials* **2022**, *15*, 2538. <https://doi.org/10.3390/ma15072538>

Academic Editor: Antonio Gil Bravo

Received: 22 February 2022

Accepted: 25 March 2022

Published: 30 March 2022

Publisher's Note: MDPI stays neutral with regard to jurisdictional claims in published maps and institutional affiliations.



Copyright: © 2022 by the authors. Licensee MDPI, Basel, Switzerland. This article is an open access article distributed under the terms and conditions of the Creative Commons Attribution (CC BY) license (<https://creativecommons.org/licenses/by/4.0/>).

1. Introduction

Global warming is a serious challenge for human activity today; it is also a global environmental issue recognized by the international community [1,2]. The main reason for global warming is the results of the rise in global population [3–5], solid wastes [6], as well as the correspondingly dramatic and continuing uptrend in the concentration of greenhouse gases worldwide, of which carbon dioxide (CO_2) is the largest contributor [7]. Three kinds of CO_2 -conversion strategies exist: electrocatalysis, thermal-catalysis, and photocatalysis, to the direct conversion of CO_2 into valuable fuel and chemical products under ambient conditions [8–11], which has attracted increasing attention from researchers [12–16]. However, the CO_2 -reduction reaction (CO_2RR) still suffers from low faradaic efficiency, low conversion efficiency, sluggish kinetics of the primary side reaction of hydrogen-evolution reaction, and high overpotential, which have greatly hindered its further practical applications. Based on this, transition-metal (TM)-based catalysts have been applied to improve the CO_2RR performance [17], as well as waste-originated biorenewables and other catalysts [18–22].

The well-noted single-atom catalyst (SAC) was first attempted to design and synthesize novel materials by defect, modification, high-temperature shockwave, and self-assembly, which have enabled various catalytic conversions, including CO₂RR with extremely higher atom efficiency, activity, and durability [23–27]. Double-atom catalysts (DACs) such as Cu-Pt [28–31], Cu-Au [32–34], and Pd-Au [35] in many mainstream reactions have also been experimented, characterized, and developed to improve CO₂-reduction-reaction efficiency, offering a fascinating catalyst model for theorists to explore, and hence gaining enormous attention. DACs usually exhibit better catalytic performance than SACs [28,34,35]. This is mainly due to their tuning diversity and synergistic effect between adjacent active sites of metal dimers, resulting in low-coordination metal atoms and an extra metal site. The interaction of different metal sites could accelerate the intrinsic CO₂RR performance of bimetallic dimer-embedded catalysts. For example, Baldoví et al. [34] loaded Au-, Cu-, and Au/Cu-alloy NPs on the surface of TiO₂. The study showed that the introduction of Cu into Au/Cu-TiO₂ could boost the transfer of the CB electrons in TiO₂ to CO₂, resulting in a higher conversion efficiency toward CO₂ reduction to CH₄. Zheng et al. [35] introduced a secondary metal (Au) to support the Pd catalyst, and Au concentration could alter the dominant reaction pathway, which was much more favorable for CO₂ reduction performance. Therefore, the combination of non-noble metals and noble metals and even the non-noble metal dimers embedded on TiO₂ substrate might be a novel and effective method to promote CO₂ adsorption and conversion.

Meanwhile, many studies [36–39] found that CO was an important intermediate in the transformation of CH₄, CH₃OH, and HCHO. The CO₂-reduction reaction can be regarded as a “series reaction”. CO₂ molecules need to be converted into CO first to obtain the target gas product. Therefore, it is a feasible strategy to design bimetallic dimer TiO₂ catalysts that can firmly adsorb CO to achieve CO₂ reduction to CH₄.

Based on the first-principles calculation, we explored CO₂ reduction on TiO₂ with M-N (M, N = Cu, Pt, Zn) dimer doping. We mainly calculated both the binding energy and charge distributions of the bimetallic dimer-embedded A-TiO₂(101) substrate and the CO₂ molecule adsorbed on these dimer-embedded A-TiO₂(101) catalysts, respectively. We also calculated the Bader charge and Charge Density Difference (CDD) from the TiO₂ substrate to the bimetallic dimer and from the bimetallic dimer-embedded TiO₂ to CO₂ gas molecule. The results indicated that the structure of the bimetallic dimer-embedded TiO₂(101) surface was stable, and the CO₂ molecule could stably stay on the bimetallic dimer-embedded TiO₂(101) surface. Then, the CO₂ reduction reactivity was proposed. The energy barrier of the Zn-Cu dimer-embedded TiO₂(101) surface was as low as 0.31 eV, which was a much more suitable choice as well as advantageous in terms of economy. Therefore, the findings of this study might theoretically provide an effective strategy for the designing of effective CO₂-reduction TiO₂-based catalysts.

2. Computational Details

Based on the density functional theory, all first-principles calculations were used in the CO₂ adsorption and reduction on the bimetallic dimer-embedded A-TiO₂(101) surface. Projected augmented-wave pseudopotentials, generalized-gradient-approximation (GGA) method [40–42], and Perdew–Burke–Ernzerhof (PBE) functional were employed using Vienna Ab-initio Simulation Package (VASP, vasp.5.4.1, Hafner team of University of Vienna, Vienna, Austria) [43–45] through the computational simulations. For the kinetic processes, the previous studies indicated that the GGA-PBE approach could correctly describe CO-oxidation, CO₂-dissociation, and O-diffusion [46,47] reaction paths on the surface. The cutoff of the kinetic energy for the plane wave was set to be 450 eV. Further, 2 × 2 × 1 was used for the Monkhorst–Pack k-point mesh during geometry optimizations, and the corresponding electronic structure calculations were set as 3 × 3 × 1. The convergence criterion for the electronic was chosen as 10^{−5} eV, and the maximum force of each atom for ionic relaxation was 0.02 eV/Å. Regarding the dissociation and diffusion of the CO₂ reduction process, the transition state (TS) search was performed by the climbing-image

nudged-elastic-band method [48–50]. Bader charge analysis was used to obtain the electronic transformation, and charge-density difference was calculated to observe its charge distribution [51].

The lattice parameters of the A-TiO₂ system were $a = 3.830 \text{ \AA}$ and $c = 9.613 \text{ \AA}$. A 3×2 surface supercell of TiO₂ with three stoichiometric (TiO₂)-structure layers was selected, of which the bottom TiO₂ layer was fixed to simulate the bulk structure and the total atom was 108, to investigate the CO₂ adsorption and dissociation performance. In the direction perpendicular to the (101) plane, the thickness of the vacuum layer was set to be 10 Å to eliminate the influence between the adjacent layers.

When Zn-Cu, Zn-Pt, and Cu-Pt dimers were embedded onto the surface of TiO₂(101), the binding energy (E_b) of this bimetallic dimer-embedded A-TiO₂(101) substrate was defined as

$$E_b = E_{\text{surface+dimer}} - E_{\text{surface}} - E_{\text{TiO}_2} \quad (1)$$

where $E_{\text{surface+dimer}}$ is the system energy of the bimetallic dimer-embedded TiO₂; E_{surface} is the system energy without bimetallic dimer; and E_{dimer} is the energy of independent bimetallic dimer.

To explore the adsorption performance of CO₂ molecules on a bimetallic dimer-embedded A-TiO₂(101) surface, the adsorption energy ($E_{\text{CO}_2\text{ad}}$) was defined as

$$E_{\text{CO}_2\text{ad}} = E_{\text{surf+CO}_2} - E_{\text{surf}} - E_{\text{CO}_2} \quad (2)$$

where $E_{\text{surf+CO}_2}$ is the system energy of adsorbed CO₂ molecules on a bimetallic dimer-embedded A-TiO₂(101) surface; E_{surf} is the system energy without the adsorbed CO₂ molecule; E_{CO_2} is the energy of the free gas molecules.

3. Results and Discussions

3.1. Bimetallic Sites on Anatase TiO₂(101) Surface

We chose three bimetallic combinations, Zn-Cu, Zn-Pt, and Cu-Pt, to observe the CO₂ adsorption and reduction on a bimetallic dimer-embedded TiO₂(101) surface. If a bimetallic dimer was embedded on the A-TiO₂(101) surface, several possible binding sites could be selected. We chose the most suitable embedded sites through several configurations of metal-embedded A-TiO₂(101), which are shown in Figure 1. The binding energy of Zn-Cu, Zn-Pt, and Cu-Pt on the surface of A-TiO₂(101) was -2.34 eV , -3.6 eV , and -2.9 eV , respectively, indicating that bimetallic-dimer interstitials could stably stay on the A-TiO₂(101) surface, along with bond length of M-N, M-O_{2c}, N-Ti and the angle of O_{2c}-M-O_{2c}, as listed in Table 1.

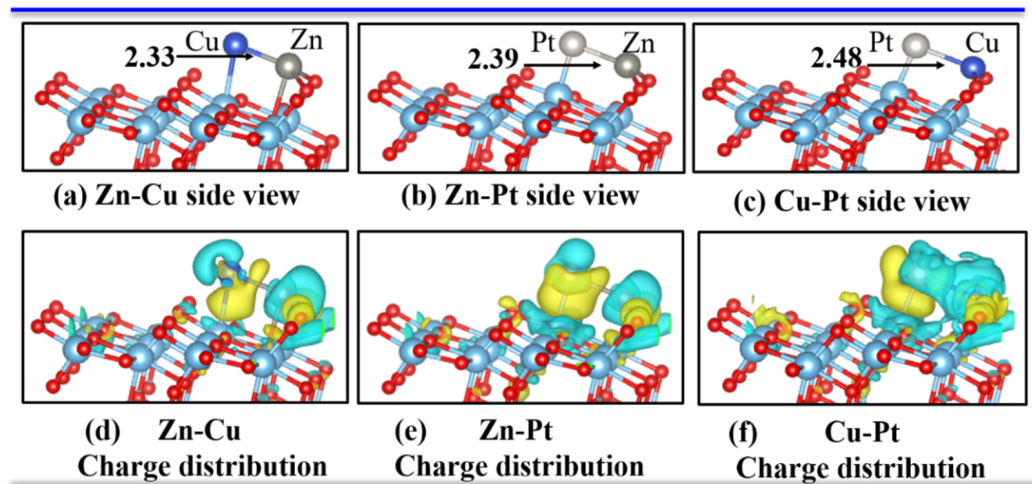


Figure 1. (a–c) Bimetallic-dimer interstitial configurations. (d–f) Charge density induced by Zn-Cu,

Zn-Pt, and Cu-Pt interstitials of the TiO₂(101) surface from a side view, respectively. The isosurface value was set as 0.0025 e/bohr³. The electron accumulation is denoted with the yellow regions; green indicates electron depletion. The Cu atom in dark blue color, Pt atom is pale, and Zn atom in light gray color.

Table 1. Calculated results for bimetal-embedded A-TiO₂ systems, including the distance d_{M-N} between two metal atoms; d_{M-O} and d_{M-N} is the distance of metal M and O₍₂₎, and Ti and metal N atom, respectively. The angle of O_{2c}-M-O_{2c} is equal to $\angle O_{2c}-M-O_{2c}$. The binding energies of bimetallic atoms on A-TiO₂(101) (E_b) and the charge transfer from A-TiO₂ to bimetallic atoms (ΔQ). M stands for the former metal atom, and N stands for the later one.

Dimer	d_{M-N} (Å)	d_{M-O} (Å)	$\angle O_{2c}-M-O_{2c}$ (°)	d_{Ti-N} (Å)	E_b (eV)	ΔQ (e)
Zn-Cu	2.32	2.07	108.42°	2.62	−2.34	−0.85
Zn-Pt	2.39	2.02	114.96°	2.28	−3.60	−0.52
Cu-Pt	2.48	1.92	135.90°	2.29	−2.90	−0.60

Bader charge analysis and CDD were also performed to further study the stability of the bimetallic dimer-embedded TiO₂ surface. As listed in Table 1, about 0.85 e, 0.52 e, and 0.60 e were transferred from the embedded Zn-Cu, Zn-Pt, and Cu-Pt dimers to the A-TiO₂(101) substrate for these three different configurations (Figure 1), respectively, which were mainly accepted by the neighboring O atoms. The interaction between embedded bimetallic dimers and A-TiO₂(101) surface led to the charge redistribution and the accumulation of electrons around the Zn-O, Zn-O, Cu-Pt bonds for Zn-Cu, Zn-Pt, and Cu-Pt dimer embedded TiO₂ systems, respectively, which could be confirmed by CDD, as shown in Figure 1d–f. Further, the partial density of states (PDOS) of three dimer-TiO₂(101) systems, as shown in Figure 2, revealed many impurity peaks induced by 2p orbital electrons of O atom and 3d orbital electrons of Zn and Cu atoms, indicating that the chemical activity of embedded TiO₂ surface was relatively stronger. Therefore, the results of PDOS, Bader charge analysis, and CDD demonstrated the formation of strong chemical bonds between Zn-Cu, Zn-Pt, Cu-Pt dimers and neighboring oxygen atoms. Therefore, the A-TiO₂(101) surface embedded with Zn-Cu, Zn-Pt, and Cu-Pt dimers were chemically stable.

3.2. One CO₂ Molecule Adsorbed on the Bimetal-TiO₂(101) Surface

When a CO₂ molecule came close to these three configuration surfaces, it will be adsorbed on the surface. Before further exploring the CO₂ adsorption and reduction on the bimetal-TiO₂(101) surface, several adsorbed sites were determined, and the most stable surface models for Zn-Cu, Zn-Pt, and Cu-Pt dimers were obtained, as shown in Figure 3. For these three configurations, the adsorption energies for CO₂ molecules of −0.15 eV, −0.17 eV, and −0.13 eV, respectively. The calculation results demonstrated weaker physical adsorption between the CO₂ molecule and bimetallic interstitial. The structure of CO₂ molecule is nearly the same with the gas state with the bond length of 1.18 Å and $\angle O_{(1)}-C-O_{(2)}$ around 180°. At the same time, the results of the charge transfer from A-TiO₂ to the bimetallic dimer showed few electrons transferring from the CO₂ molecules to the dimer-embedded TiO₂ substrate, namely 0.03 e, 0.02 e, and 0.02 e for Zn-Cu, Zn-Pt, and Cu-Pt dimer-embedded TiO₂(101) systems, respectively. Thus, the interactions between the CO₂ molecule and the dimer-embedded A-TiO₂(101) surface were relatively weaker. All these results showed a weaker physical absorption between the system and CO₂ molecules.

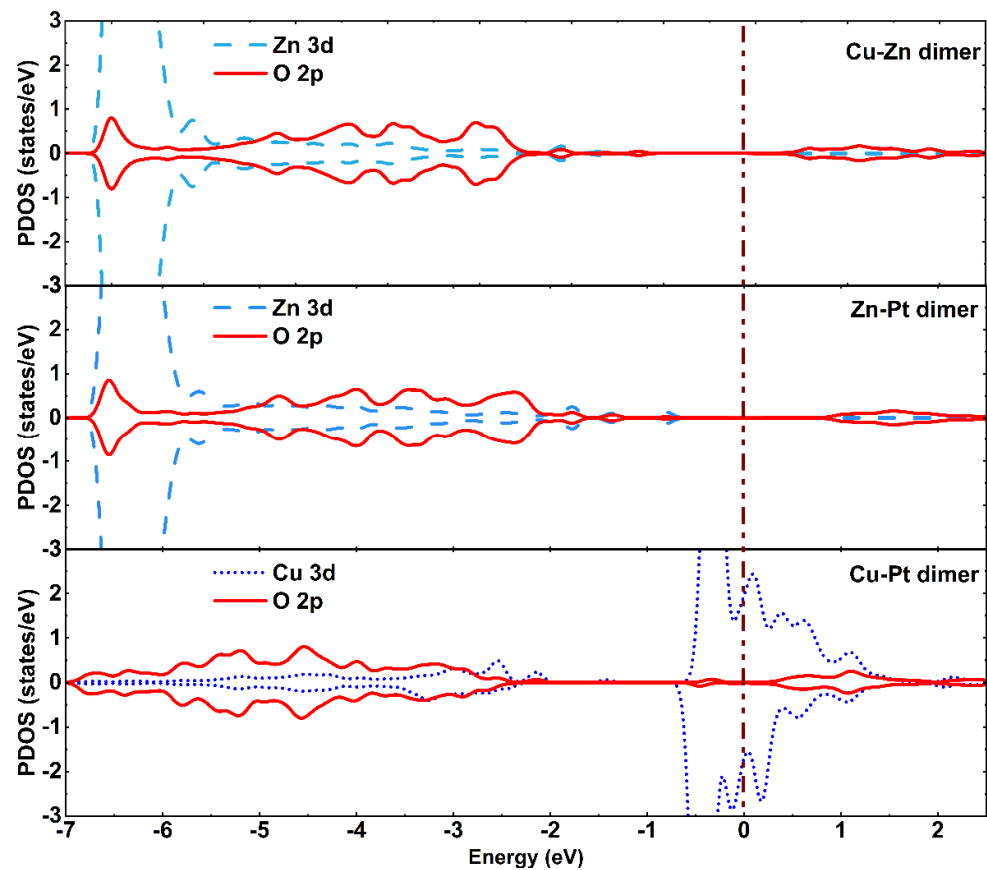


Figure 2. Partial density of states for the bimetal-TiO₂ system (bimetallic dimers are Zn-Cu, Zn-Pt, and Cu-Pt). The Fermi level was set to zero and is marked with a grown dashed line.

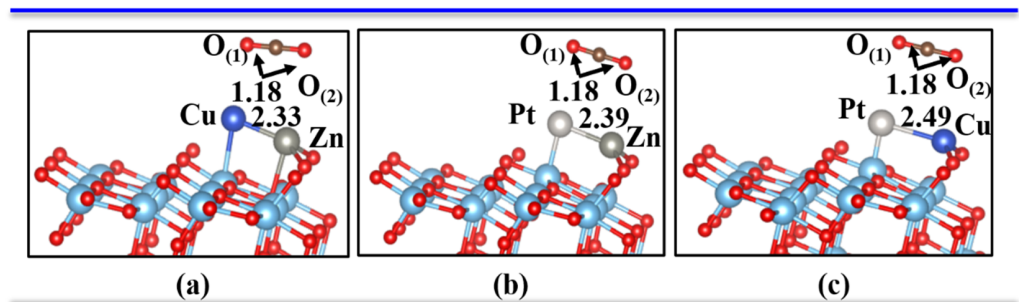


Figure 3. One CO₂ molecule adsorbed on the surface of the bimetal-TiO₂(101) system from a side view. (a–c) are Cu-Zn, Pt-Zn and Pt-Cu, respectively.

Meanwhile, the CO₂ gas molecule was more stably adsorbed onto the bimetal-embedded TiO₂ surface with a small barrier energy, which was about 0.03 eV, 0.23 eV, and 0.12 eV for the Zn-Cu, Zn-Pt, and Cu-Pt series, respectively. The final stable adsorbed structures are shown in Figure 4a–c. Moreover, the charge distribution from CDD is shown in Figure 4d–f. As shown in Figure 4, the CO₂ molecules were bound to the dimer-TiO₂(101) system via the bimetallic atoms. The distances between the C atom and the nearest embedded metal of the dimer-TiO₂ substrate were shortened to be 1.87 Å, 2.00 Å, and 1.99 Å for Zn-Cu, Zn-Pt, and Cu-Pt adsorption cases, respectively, which were much nearer than those of the initial adsorption cases. Moreover, the bonds of O₍₁₎-C and C-O₍₂₎ were enlarged to be about 1.24 Å and 1.30 Å, respectively, and the adsorption energies were elevated up to −0.36 eV, −0.46 eV, and −0.97 eV for Zn-Cu, Zn-Pt, and Cu-Pt cases, respectively. Therefore,

the adsorption of CO₂ molecules on the dimer-TiO₂(101) surface should be a chemical adsorption behavior.

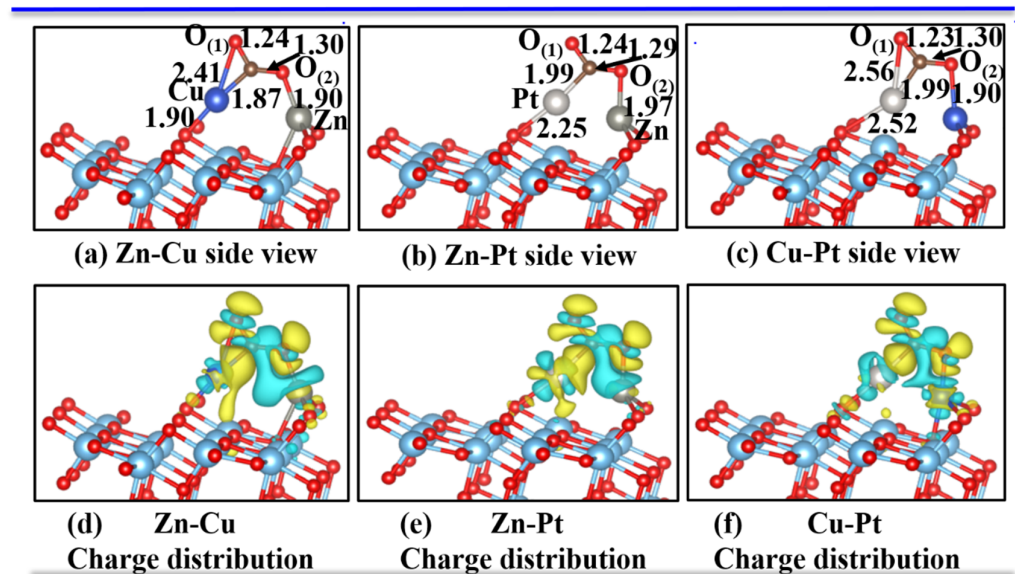


Figure 4. Most stable configurations (a–c) and the corresponding charge-density differences (d–f) of a CO₂ molecule adsorbed on the Zn-Cu, Zn-Pt, and Cu-Pt dimer-embedded A-TiO₂(101) surface from a side view. The isosurface value was set as 0.0025 e/bohr³. The electron accumulation is denoted with the yellow regions, while the electron depletion is denoted with green regions. The Cu atom in dark blue color, Pt atom is pale, and Zn atom in light gray.

The partial densities of states of the adsorbed CO₂ on the bimetallic dimer-embedded TiO₂ system (bimetallic dimers were Zn-Cu, Zn-Pt, and Cu-Pt) were calculated to further understand this adsorption performance, which are shown in Figure 5. When CO₂ molecules were adsorbed on the bimetal-embedded TiO₂ surface, we could clearly observe the hybridization with the orbitals of adsorbed CO₂ molecules and 3d orbitals of dopant Zn, Cu, and Pt atoms, implying the formation of Zn-O, Cu-O, and Pt-O bonds on the interface between the adsorbed CO₂ molecules and the dimer-TiO₂ system. Moreover, the Bader charge analysis revealed about 0.82 e, 0.67 e, and 0.54 e transferred from the CO₂ molecules to the dimer-embedded TiO₂ substrate for Zn-Cu, Zn-Pt, and Cu-Pt dimers (see Table 2). In addition to the calculations of charge distribution, we could see that the accumulation of charge occurred around metal-O bonds; the CDD is plotted in Figure 4d–f. The results of the charge transfer and charge redistribution demonstrated the strong chemical interaction between the dopant dimer of Zn-Cu, Zn-Pt, and Cu-Pt and nearby O adatoms, namely Zn-O, Zn-O, and Cu-O bonds. This might be the reason for the increase in O₍₁₎-C and C-O₍₂₎ bond lengths. Further, we found that the adsorption energy of the Cu-Pt-TiO₂ system was relatively higher, which was two times more than that of other two cases. The absolute value of charge transfer for the Zn-Cu-TiO₂ system, as well as the extents of overlap of electronic states was also larger. Therefore, the aforementioned results, especially the structural variation and charge redistribution of CO₂ molecules and different dimer-TiO₂ substrates, showed stronger chemical interaction between CO₂ molecules and dimer-embedded TiO₂(101) surface. Thus, CO₂ molecules could stably stay and were chemically adsorbed. The details of initial physical adsorption to final chemical adsorption, along with the reduction process, were as follows.

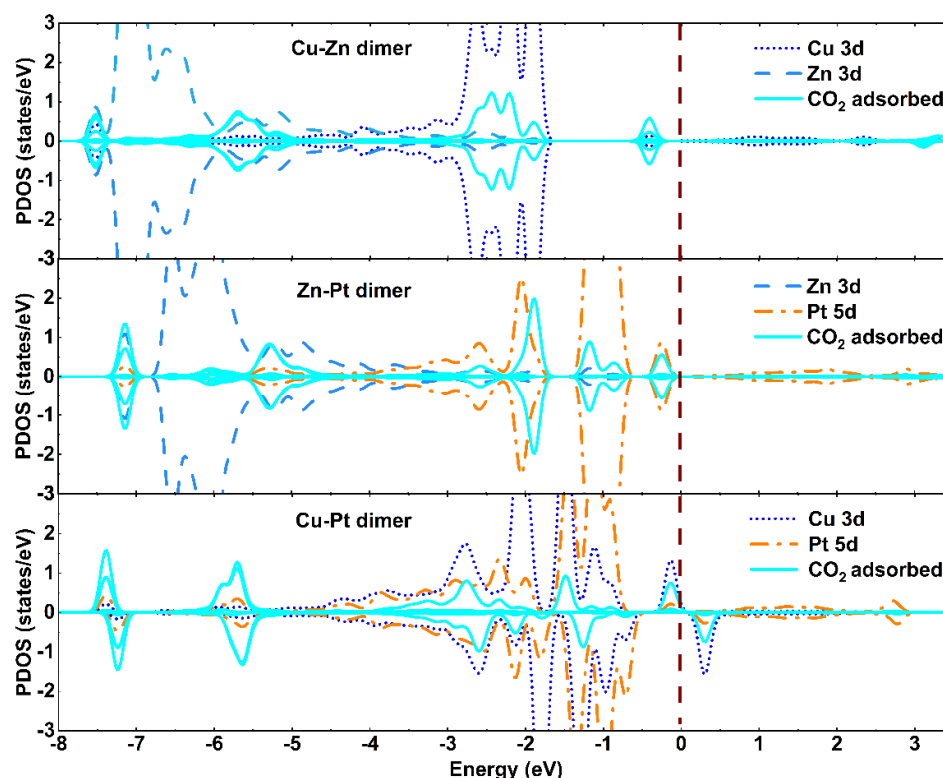


Figure 5. Partial density of states of the absorbed CO₂ on bimetal-embedded TiO₂ system (bimetallic dimers were Zn-Cu, Zn-Pt, and Cu-Pt). The Fermi level was set to zero and is marked with a grown dashed line.

Table 2. Calculated results for a CO₂ molecule on an A-TiO₂(101) surface during the adsorption process. d_{M-N} and $d_{O(1)-C}$ are the bond lengths between metal M and metal N, and between the O₍₁₎ atom and the C atom, respectively, for chemical adsorption structure. E_{CO_2ads} stands for the adsorption energy of CO₂ adsorbed on TiO₂(101) surface. ΔQ is the charge transfer from bimetallic dimer-embedded TiO₂ to CO₂ molecule. M stands for the former metal atom, and N stands for the latter one.

	d_{M-N} (Å)	$d_{M-O(2)}$ (Å)	$d_{O(1)-C}$ (Å)	$d_{C-O(2)}$ (Å)	$\angle O_{2c}-M-O_{2c}$ (°)	d_{C-N} (Å)	$d_{O_{2c}-N}$ (Å)	E_{CO_2ads} (eV)	ΔQ (e)
Pure TiO ₂	-	-	1.18	1.18	180	-	-	-0.31	-
Zn-Cu	3.45	1.90	1.24	1.30	125.92	1.87	1.90	-0.36	0.82
Zn-Pt	2.68	1.97	1.24	1.29	130.90	1.99	2.25	-0.46	0.67
Cu-Pt	2.63	1.90	1.23	1.30	132.32	1.99	2.52	-0.97	0.54

3.3. CO₂ Reduction on the Zn-Cu, Zn-Pt, and Cu-Pt Dimer-Embedded Anatase TiO₂(101) Surface

After determining the structure and CO₂ adsorption of bimetallic dimer-embedded on the A-TiO₂(101) surface, we first discussed the effect of the Zn-Cu dimer-embedded A-TiO₂(101) substrate on the reduction of the CO₂ molecule. We chose the direct reduction pathway. We determined the optimized structures of the TSs across dissociation and diffusion processes, as well as the products involved in this pathway, which are shown in Figure 6. For the Zn-Cu-CO₂ system, CO₂ molecules subsequently dissociated into the adsorbed *CO of the O-C-Cu bond and *O* bonded with Cu, Zn, and Ti atoms onto the surface via the transition states TS1, TS2, and TS3 and intermediate states A2 and A3. The asterisk (*) is denoted as the adsorbed sites. When a CO₂ molecule was adsorbed on the surface of the Zn-Cu dimer-embedded A-TiO₂(101) surface, the Cu and Zn atoms could diffuse to adsorb the CO₂ molecule and the Zn-Cu bond was broken, which resulted in

the formation of new bonds of Cu-O₍₁₎, Cu-C, Cu-Ti, and Zn-O₍₂₎. The energy barrier for TS1 was only 0.03 eV, and then the CO₂ molecule could be stably adsorbed onto the surface of the TiO₂ system.

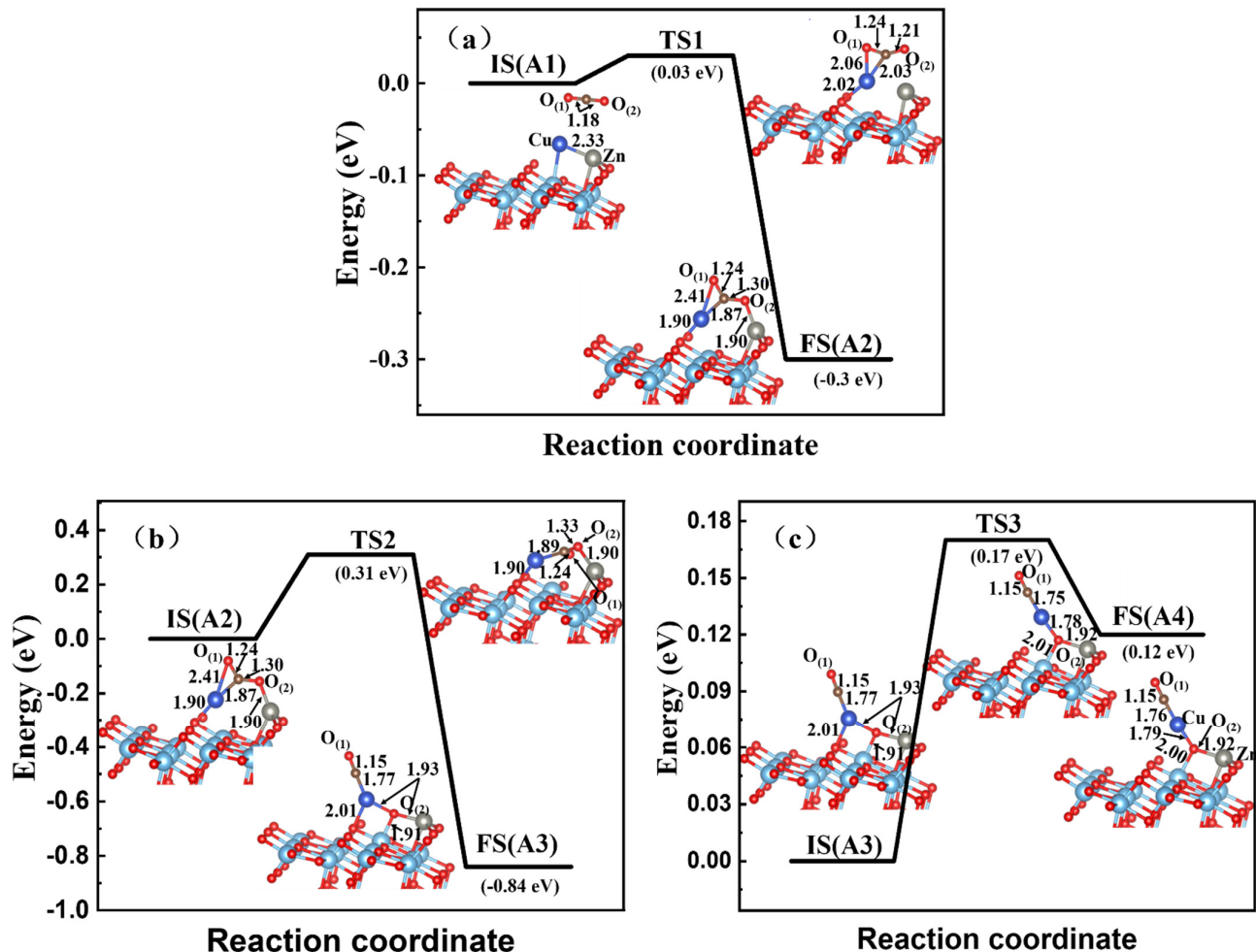


Figure 6. CO₂ reduction on the Zn-Cu-embedded A-TiO₂(101) surface. For the A-TiO₂ system, the bond unit was Å. The Cu atom in dark blue, and Zn atom in light gray. (a) is the adsorption process, (b,c) are the two steps of reduction process.

As shown in Figure 6b, A2 was the initial configuration and the CO₂ gas phase dissociated. A lower energy of 0.31 eV was needed for the dissociation step. In this step, the O₍₁₎ atom diffused away and led to the breaking of the Cu-O₍₁₎ bond, while the O₍₂₎ atom moved a little nearer and then bonded with Cu, Zn, and Ti atoms, which were much closer to the A-TiO₂(101) surface through TS2. With a decrease of 0.84 eV, the Zn-Cu-TiO₂(101) system achieved a more stable structure than A2 after this transformation. However, A3 was a metastable configuration, since C and O₍₂₎ from the gas phase exhibited more polarity. The interaction with the surface Cu atom was enhanced, and the more active atom of embedded Cu easily diffused outward to be adsorbed by OC* to a more stable site by an energetic driving force. With a tiny energy barrier of 0.17 eV, the diffusion of A3 transforming into A4 was achieved easily. As a result, with the breaking of the Cu-Ti bond, the new bonds of O₍₁₎-C, C-Cu, and Cu-O₍₂₎ were aligned in a straight line with the bond lengths of 1.15 Å, 1.76 Å, and 1.79 Å. For the whole reaction process of A1 → A2 → A3 → A4 (Figure 6), the highest-energy barrier and the total reaction energy of CO₂ reduction on the Zn-Cu-TiO₂ system were 0.31 eV and 0.72 eV, respectively, corresponding to the transformation from A2 to A4. The results indicated that the reaction of CO₂ dissociation became much easier

with the help of the Zn-Cu dimer embedded on the A-TiO₂(101) surface. The embedded dimer might also contribute a more active site on the surface and improve the CO₂ reduction behaviors. Meanwhile, the configuration structure also became more stable upon CO₂ adsorption and reduction reaction on the dimer-embedded A-TiO₂ surface.

After a CO₂ molecule was adsorbed on the A-TiO₂(101) surface, the structure B1 was first obtained easily without nearly any difference with the independent CO₂ gas phase and the Zn-Pt-TiO₂ system, as shown in Figure 1b, indicating the physical adsorption of the stable structure B1. For the structure B1, the embedded Zn and Pt atoms were particularly prone to adsorb CO₂ molecules. Then, a much more stable structure B2 was obtained through TS4 with an energy barrier of 0.23 eV (Figure 7a); the system energy slightly decreased by 0.28 eV. As a result, the two new bonds of Pt-C and Zn-O₍₂₎ were formed, and the adsorption energy of the CO₂ molecule increased to −0.46 eV. The adsorbed CO₂ molecule on the surface became much more stable via chemical adsorption. For B2 as the initial configuration, the adsorbed CO₂ molecule was dissociated on the Zn-Pt dimer-embedded TiO₂(101) surface, as shown in Figure 7b. The dissociation energy barrier of the adsorbed CO₂ molecule was 1.69 eV, which was much higher than that in the Zn-Cu case, as shown in Figure 6b. In the transition state TS5, the adsorbed CO₂ molecule was dissociated, along with the breaking of C-O₍₂₎ and Pt-Ti bonds and the formation of new bonds of Pt-O₍₂₎ and Pt-O_{3c} on the subsurface. For the whole reaction path of C1 → TS4 → C2 → TS5 → C3, the highest-energy barrier was 1.69 eV, and the system energy decreased by 0.9 eV. The results also demonstrated that the dissociated CO was stably adsorbed on the Zn-Pt dimer-embedded TiO₂(101) surface, and the final structure B3 also became much more stable.

For the Cu-Pt case, the structures C1 and C4 were initial and final configurations; the dissociation-reaction energy and energy barrier were −1.34 eV and 1.58 eV, respectively. Similarly to the former two dimer-embedded TiO₂(101) surfaces, a more stable structure, C2, was obtained with a lower-energy barrier of 0.12 eV. Obviously, the new Pt-C and Cu-O₍₂₎ chemical bonds of 1.99 Å and 1.90 Å, were formed. The C-O₍₂₎ bond was strengthened to be 1.30 Å with a small bend of CO₂ molecules, while the Cu-Pt bond was broken. Subsequently, the adsorbed CO₂ molecule began to dissociate, as shown in Figure 8b. In the transition state TS7, the C-O₍₂₎ bond of the CO₂ molecule was initially broken, with a dissociation-energy barrier of 1.58 eV. As a result, O₍₂₎ atoms moved nearer to the TiO₂(101) surface, and a relatively more stable structure C3 was obtained, along with the formation of new bonds of O₍₂₎-Cu, O₍₂₎-Pt, and O₍₂₎-Ti. At the same time, C3 was a metastable configuration. The Pt atom could easily move out to be grabbed by the *CO adatom during TS7 and TS8 with the distance varying from 1.99 Å, 1.85 Å to 1.82 Å via an energetic driving force. Via the diffusion of TS8, the embedded Pt atom of structure C4 was more attracted to the *CO adatom with exothermic energy and energy barrier of 0.18 eV and 0.7 eV, respectively. For the C1 → C2 → C3 → C4 reaction path (Figure 8), the highest dissociation energy barrier was 1.59 eV, between those of TS5 and TS2 (TS2: 0.31 and TS5: 1.69 eV, respectively). The total energy of structure C4 was reduced by 1.34 eV, which was much higher than that of the two former systems. It showed that with the help of Cu-Pt dimer atoms, the dissociation process of CO₂ on the A-TiO₂(101) surface also required a relatively high-energy barrier.

We studied the adsorption and reduction performance of CO₂ molecules on three configurations of bimetallic dimer-embedded TiO₂(101): Zn-Cu, Zn-Pt, and Cu-Pt. We found unpaired electrons induced by the transfer of the bimetallic dimer to the O atom of the TiO₂ substrate. While a CO₂ molecule appeared on the TiO₂(101) surface, a partial excess charge of the bimetallic dimer was used to absorb the CO₂ gas molecule. However, the adsorption energy was relatively low, indicating only weaker physical adsorption. The final product was mainly CO, with the O atom bonded with the surrounding metal atom due to the CO₂-dissociation process on the bimetallic dimer-embedded TiO₂(101) surface.

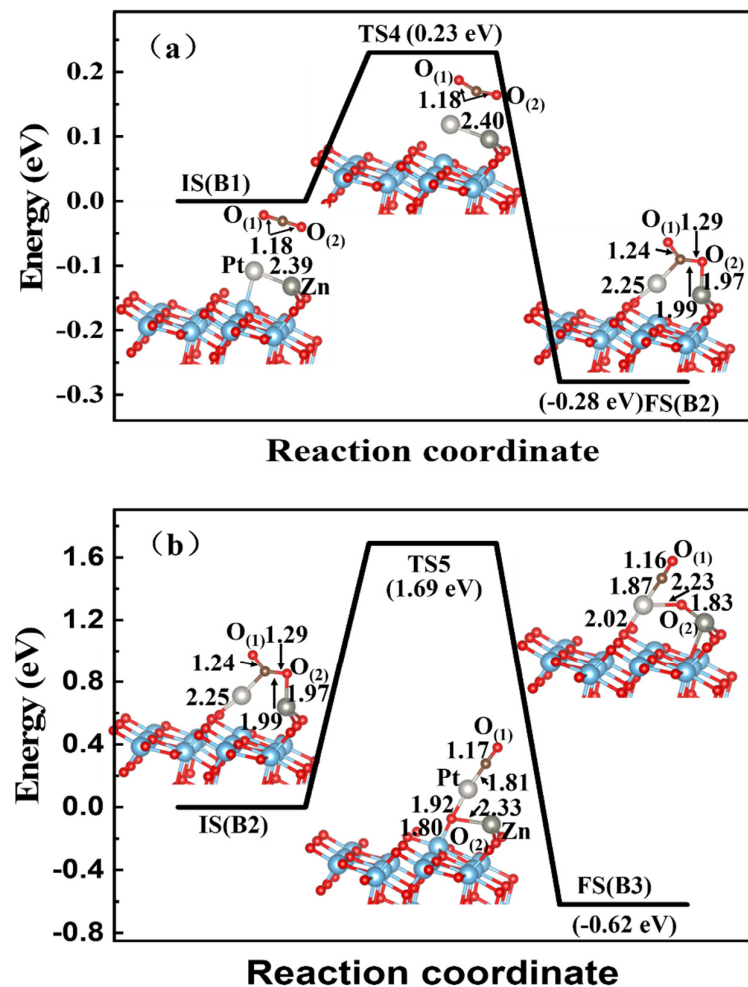


Figure 7. CO₂ reduction on Zn-Pt-embedded A-TiO₂(101) surface. The Cu atom in dark blue, Pt atom is pale, and Zn atom in light gray. (a) is the adsorption process, and (b) is the reduction process.

For the CO₂ reduction process on the Zn-Cu-embedded TiO₂(101) surface, the highest-energy barrier was as low as 0.31 eV with the breaking of the C-O₍₂₎ bond and the formation of Cu-O₍₂₎, Zn-O₍₂₎, and Ti-O₍₂₎ bonds, which was relatively suitable to produce CO and O adatoms easily. However, relatively higher-energy barriers existed for Zn-Pt and Cu-Pt dimer-embedded TiO₂(101) systems, namely 1.69 eV and 1.58 eV, respectively. As shown in Figures 7b and 8b, the C-O₍₂₎ bonds of these two systems were also broken, besides the formation of three metal-O₍₂₎ bonds. However, the Zn-Pt-TiO₂ system had higher reaction energy of 0.62 eV, promoting thermal-catalytic performance. With lower barrier energy of 0.31 eV, the Zn-Cu dimer-embedded TiO₂(101) surface might be a much more convenient design for the CO₂RR of the bimetallic dimer-embedded TiO₂ substrate, as well as a more economical method compared with noble metals such as Pt, Au, and Ag. Therefore, the findings of this study might theoretically provide an effective strategy for the designing of effective CO₂-reduction TiO₂-based catalysts.

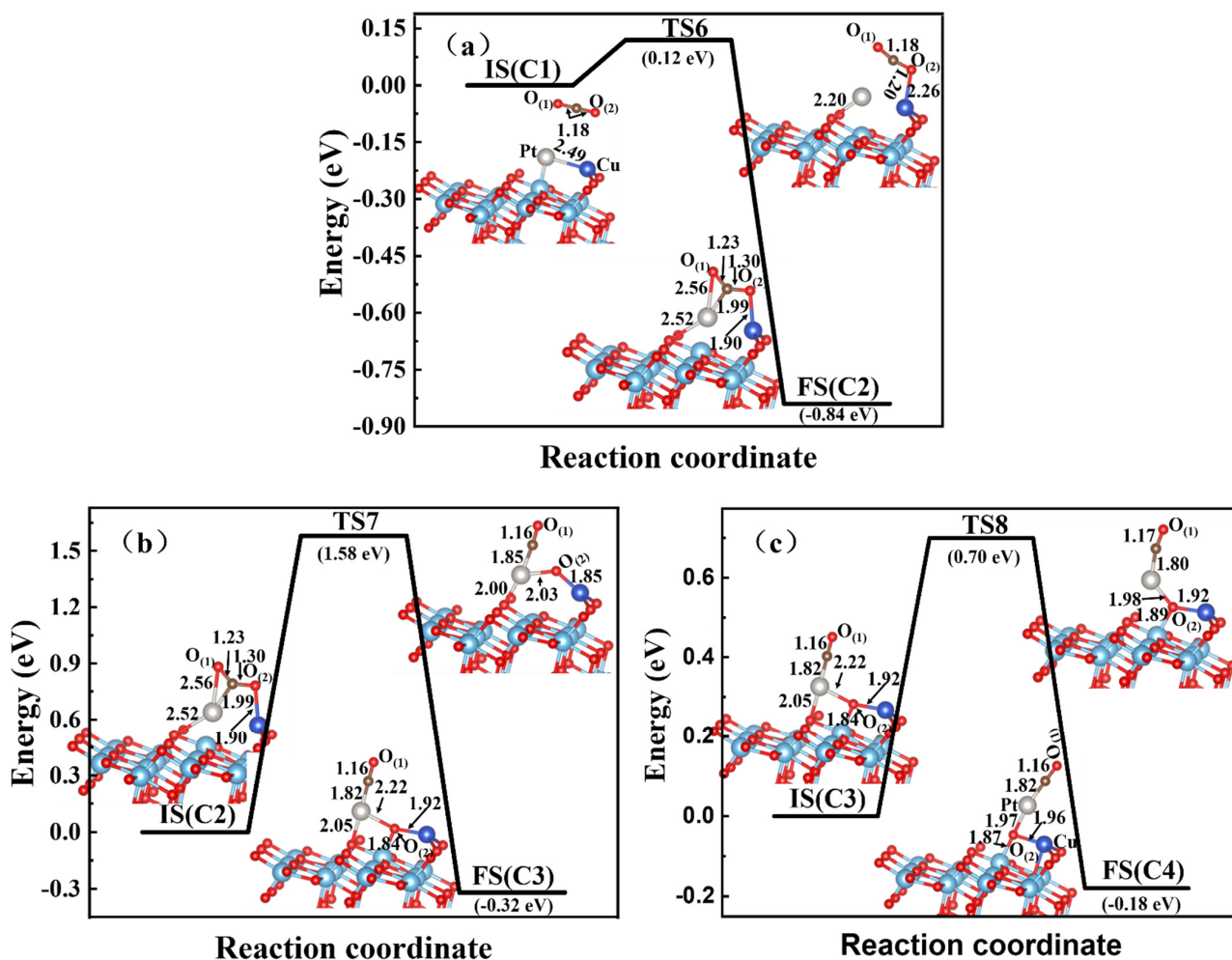


Figure 8. CO₂ reduction on the Cu-Pt-embedded A-TiO₂(101) surface. The Cu atom in dark blue, Pt atom is pale, and Zn atom in light gray. (a) is the adsorption process, (b) and (c) are the two steps of reduction process.

4. Conclusions

In this study, the enhancing effects of the Zn-Cu, Zn-Pt, and Cu-Pt dimers on the CO₂-reduction reaction of the A-TiO₂(101) surface were discussed. When the bimetallic dimer was embedded on the TiO₂(101) surface, the configuration was relatively more stable with higher binding energy. Meanwhile, the adsorption energy of CO₂ molecules on the bimetallic dimer-embedded TiO₂(101) surface was relatively lower, indicating a weaker interaction. Moreover, the Bader charge analysis exhibited only 0.03 e transferring from the CO₂ molecule to the bimetal-embedded TiO₂(101) surface, demonstrating only physical adsorption behavior. After a lower-energy barrier, the higher adsorption energy was up to -0.46 eV for the Zn-Pt-TiO₂ system and 0.82 eV of the Zn-Cu-TiO₂ system, respectively. Furthermore, the surface-electronic states also implied stronger interaction between CO₂ molecules and the bimetallic dimer-embedded TiO₂(101) surface.

Regarding the CO₂ dissociation process, the results showed that the dissociation barriers of the CO₂ molecule with Zn-Cu, Zn-Pt, and Cu-Pt dimers embedded on the TiO₂(101) surface had the values of 0.31 eV, 1.69 eV, and 1.58 eV, respectively, which benefited the CO₂-reduction reaction (CO₂RR) activity. Meanwhile, it was observed that the products *CO and *O* of CO₂ reduction were firmly adsorbed on the dimer-embedded TiO₂(101) surface. In addition, the bonds of metal-O₍₂₎-metal were less than 2.00 Å, and metal-C and C-O₍₁₎ bonds were relatively shortened to be 1.76 Å and 1.15 Å, respectively. From the viewpoint of the activation barrier and reaction energy, the Zn-Cu dimer-embedded

TiO₂(101) substrate was more favorable for CO₂ direct reduction than the other two kinds of bimetallic dimer-embedded TiO₂(101) surfaces. Meanwhile, compared with partial noble atoms such as Pt, Au, and Ag, the combination of Zn and Cu atoms was a much more suitable choice, as well as being advantageous in terms of economy with the energy barrier of 0.31 eV. Therefore, our study theoretically provided a new design of the high CO₂RR performance of Zn-Cu dimer-embedded A-TiO₂ substrate catalysts.

Author Contributions: Writing—original draft preparation, C.L.; writing—review and editing, C.L.; software, C.S.; First-Principles calculation, L.L. and B.Z.; data curation, G.Z.; picture processing, W.Y.; general guidance, Z.C. All authors have read and agreed to the published version of the manuscript.

Funding: This project was supported by the National Natural Science Foundation of China (Grant Nos. 11805295 and 11804311), the key scientific and technological project of Henan Province (Grant Nos. 212102210490, 222102230087) and the funding scheme for young backbone teachers of Zhongyuan University of Technology (Grant No. 2018XQG17).

Institutional Review Board Statement: Not applicable.

Informed Consent Statement: Not applicable.

Data Availability Statement: The data presented in this study are available within the article.

Conflicts of Interest: The authors declare that they have no known competing financial interests or personal relationships that could have appeared to influence the work reported in this paper.

References

1. USDC. *Trends in Atmospheric Carbon Dioxide, Monthly Average Mauna Loa CO₂*; National Oceanic and Atmospheric Administration: Silver Spring, MD, USA; Earth System Research Laboratory: Boulder, CO, USA; Global Monitoring Division: Boulder, CO, USA; United States Department of Commerce: Washington, DC, USA, 2021. Available online: <https://gml.noaa.gov/ccgg/trends/> (accessed on 17 July 2021).
2. Manojkumar, N.; Srimuruganandam, B. Size-segregated particulate matter and health effects in air pollution in India: A review. *Environ. Chem. Lett.* **2021**, *19*, 3837–3858. [[CrossRef](#)]
3. Desa, U. *World Population Prospects 2019: Highlights*; United Nations Department for Economic and Social Affairs: New York, NY, USA, 2019.
4. Millati, R.C.; Ariyanto, T.; Azzahrani, I.N.; Putri, R.U.; Taherzadeh, M.J. *Sustainable Resource Recovery and Zero Waste Approaches*; Elsevier: New York, NY, USA, 2019.
5. Khanal, S.K.; Varjani, S.; Lin, C.S.K.; Awasthi, M.K. Waste-to-resources: Opportunities and challenges. *Bioresour. Technol.* **2020**, *317*, 123987. [[CrossRef](#)] [[PubMed](#)]
6. Abdel-Shafy, H.I.; Mansour, M.S.M. Solid waste issue: Sources, composition, disposal, recycling, and valorization. *Egypt J. Petrol.* **2018**, *27*, 1275–1290. [[CrossRef](#)]
7. Hussain, M.; Liu, G.; Yousaf, B.; Ahmed, R.; Uzma, F.; Ali, M.U.; Ullah, H.; Butt, A.R. Regional and sectoral assessment on climate-change in Pakistan: Social norms and indigenous perceptions on climate-change adaptation and mitigation in relation to global context. *J. Clean. Prod.* **2018**, *200*, 791–808. [[CrossRef](#)]
8. Mustafa, A.; Lougou, B.G.; Shuai, Y.; Wang, Z.; Tan, H. Current technology development for CO₂ utilization into solar fuels and chemicals: A review. *J. Energy Chem.* **2020**, *49*, 96–123. [[CrossRef](#)]
9. Tackett, B.M.; Gomez, E.; Chen, J.G. Net reduction of CO₂ via its thermocatalytic and electrocatalytic transformation reactions in standard and hybrid processes. *Nat. Catal.* **2019**, *2*, 381–386. [[CrossRef](#)]
10. Huang, B.; Wu, Y.; Luo, Y.; Zhou, N. Double atom-anchored Defective Boron Nitride catalyst for efficient electroreduction of CO₂ to CH₄: A first principles study. *Chem. Phys. Lett.* **2020**, *756*, 137852. [[CrossRef](#)]
11. Liu, Z.; Sun, Z. Reductive Transformation of Carbon Dioxide. *Acta Phys. Chim. Sin.* **2021**, *37*, 2012024. [[CrossRef](#)]
12. Gao, D.; Zhang, Y.; Zhou, Z.; Cai, F.; Zhao, X.; Huang, W.; Li, Y.; Zhu, J.; Liu, P.; Yang, F.; et al. Enhancing CO₂ Electroreduction with the Metal–Oxide Interface. *J. Am. Chem. Soc.* **2017**, *139*, 5652–5655. [[CrossRef](#)]
13. Kim, D.; Resasco, J.; Yu, Y.; Asiri, A.M.; Yang, P. Synergistic geometric and electronic effects for electrochemical reduction of carbon dioxide using gold–copper bimetallic nanoparticles. *Nat. Commun.* **2014**, *5*, 4948. [[CrossRef](#)]
14. Liu, C.; Yang, B.; Tyo, E.; Seifert, S.; DeBartolo, J.; von Issendorff, B.; Zapol, P.; Vajda, S.; Curtiss, L.A. Carbon Dioxide Conversion to Methanol over Size-Selected Cu₄ Clusters at Low Pressures. *J. Am. Chem. Soc.* **2015**, *137*, 8676–8679. [[CrossRef](#)] [[PubMed](#)]
15. Bai, S.; Shao, Q.; Wang, P.; Dai, Q.; Wang, X.; Huang, X. Highly Active and Selective Hydrogenation of CO₂ to Ethanol by Ordered Pd–Cu Nanoparticles. *J. Am. Chem. Soc.* **2017**, *139*, 6827–6830. [[CrossRef](#)]
16. Lakshmidevi, J.; Ramesh Naidu, B.; Venkateswarlu, K. A rapid-room temperature synthesis of α -cyanoacrylates, α -cyanoacrylonitriles and 4H-pyrans using water extract of pomegranate ash as catalytic media. *Sustain. Chem. Pharm.* **2022**, *25*, 100610. [[CrossRef](#)]

17. Wang, Z.; Hong, J.; Ng, S.-F.; Liu, W.; Huang, J.; Chen, P.; Ong, W.-J. Recent Progress of Perovskite Oxide in Emerging Photocatalysis Landscape: Water Splitting, CO₂ Reduction, and N₂ Fixation. *Acta Phys. Chim. Sin.* **2020**, *37*, 2011033. [[CrossRef](#)]
18. Naidu, B.R.; Lakshmi Devi, J.; Naik, B.S.S.; Venkateswarlu, K. Water extract of pomegranate ash as waste-originated biorenewable catalyst for the novel synthesis of chiral tert-butanefulfinyl aldimines in water. *Mol. Catal.* **2021**, *511*, 111719. [[CrossRef](#)]
19. Appa, R.M.; Naidu, B.R.; Venkateswarlu, D.; Hanafiah, M.M.; Lakkaboyana, S.K.; Lakshmi Devi, J.; Venkateswarlu, K. Water extract of pomegranate ash–I2 as sustainable system for external oxidant/metal/catalyst-free oxidative iodination of (hetero)arenes. *Green Chem. Lett. Rev.* **2021**, *14*, 700–712. [[CrossRef](#)]
20. Di Giovannantonio, M.; Kosmala, T.; Bonanni, B.; Serrano, G.; Zema, N.; Turchini, S.; Catone, D.; Wandelt, K.; Pasini, D.; Contini, G.; et al. Surface-Enhanced Polymerization via Schiff-Base Coupling at the Solid–Water Interface under pH Control. *J. Phys. Chem. C* **2015**, *119*, 19228–19235. [[CrossRef](#)]
21. Di Giovannantonio, M.; El Garah, M.; Lipton-Duffin, J.; Meunier, V.; Cardenas, L.; Revurat, Y.F.; Cossaro, A.; Verdini, A.; Perepichka, D.F.; Rosei, F.; et al. Insight into Organometallic Intermediate and Its Evolution to Covalent Bonding in Surface-Confined Ullmann Polymerization. *ACS Nano* **2013**, *7*, 8190–8198. [[CrossRef](#)]
22. Klopp, J.M.; Pasini, D.; Byers, J.D.; Willson, C.G.; Frechet, J.M.J. Microlithographic assessment of a novel family of transparent and etch-resistant chemically amplified 193-nm resists based on cyclopolymers. *Chem. Mater.* **2001**, *13*, 4147–4153. [[CrossRef](#)]
23. Lakshmi Devi, J.; Vakati, V.; Naidu, B.R.; Raghavender, M.; Rao, K.S.V.K.; Venkateswarlu, K. Pd(5%)-KIT-6, Pd(5%)-SBA-15 and Pd(5%)-SBA-16 catalysts in water extract of pomegranate ash: A case study in heterogenization of Suzuki-Miyaura reaction under external base and ligand free conditions. *Sustain. Chem. Pharm.* **2021**, *19*, 100371. [[CrossRef](#)]
24. Zhou, X. TiO₂ Supported Single-Atom Catalysts for Photocatalytic Reactions. *Acta Phys. Chim. Sin.* **2020**, *37*, 2008064. [[CrossRef](#)]
25. Cai, S.; Wang, L.; Heng, S.; Li, H.; Bai, Y.; Dang, D.; Wang, Q.; Zhang, P.; He, C. Interaction of Single-Atom Platinum–Oxygen Vacancy Defects for the Boosted Photosplitting Water H₂ Evolution and CO₂ Photoreduction: Experimental and Theoretical Study. *J. Phys. Chem. C* **2020**, *124*, 24566–24579. [[CrossRef](#)]
26. Huang, L.; Li, W.; Zeng, M.; He, G.; Shearing, P.R.; Parkin, I.P.; Brett, D.J.L. Metal-Nitrogen-doped carbon single-atom electrocatalysts for CO₂ electroreduction. *Compos. Part. B Eng.* **2021**, *220*, 108986. [[CrossRef](#)]
27. Liu, J. Catalysis by Supported Single Metal Atoms. *ACS Catal.* **2016**, *7*, 34–59. [[CrossRef](#)]
28. Lang, Q.; Yang, Y.; Zhu, Y.; Hu, W.; Jiang, W.; Zhong, S.; Gong, P.; Teng, B.; Zhao, L.; Bai, S. High-index facet engineering of PtCu cocatalysts for superior photocatalytic reduction of CO₂ to CH₄. *J. Mater. Chem. A* **2017**, *5*, 6686–6694. [[CrossRef](#)]
29. Li, A.; Wang, T.; Chang, X.; Zhao, Z.-J.; Li, C.; Huang, Z.; Yang, P.; Zhou, G.; Gong, J. Tunable syngas production from photocatalytic CO₂ reduction with mitigated charge recombination driven by spatially separated cocatalysts. *Chem. Sci.* **2018**, *9*, 5334–5340. [[CrossRef](#)]
30. Zhang, X.; Han, F.; Shi, B.; Farsinezhad, S.; Dechaine, G.P.; Shankar, K. Photocatalytic Conversion of Diluted CO₂ into Light Hydrocarbons Using Periodically Modulated Multiwalled Nanotube Arrays. *Angew. Chem. Int. Ed.* **2012**, *51*, 12732–12735. [[CrossRef](#)]
31. Lee, S.; Jeong, S.; Kim, W.D.; Lee, S.; Lee, K.; Bae, W.K.; Moon, J.H.; Lee, S.; Lee, D.C. Low-coordinated surface atoms of CuPt alloy cocatalysts on TiO₂ for enhanced photocatalytic conversion of CO₂. *Nanoscale* **2016**, *8*, 10043–10048. [[CrossRef](#)]
32. Neațu, Ș.; Maciá-Agulló, J.A.; Concepción, P.; Garcia, H. Gold–Copper Nanoalloys Supported on TiO₂ as Photocatalysts for CO₂ Reduction by Water. *J. Am. Chem. Soc.* **2014**, *136*, 15969–15976. [[CrossRef](#)]
33. Kang, Q.; Wang, T.; Li, P.; Liu, L.; Chang, K.; Li, M.; Ye, J. Photocatalytic reduction of carbon dioxide by hydrous hydrazine over Au-Cu alloy nanoparticles supported on SrTiO₃/TiO₂ coaxial nanotube arrays. *Angew. Chem. Int. Ed.* **2015**, *54*, 841–845. [[CrossRef](#)]
34. Baldoví, H.G.; Neațu, Ș.; Khan, A.; Asiri, A.M.; Kosa, S.A.; Garcia, H. Understanding the Origin of the Photocatalytic CO₂ Reduction by Au- and Cu-Loaded TiO₂: A Microsecond Transient Absorption Spectroscopy Study. *J. Phys. Chem. C* **2015**, *119*, 6819–6827. [[CrossRef](#)]
35. Zheng, M.; Jia, C.; Sharman, E.; Jiang, J.; Fan, W.; Zhao, X. Maximizing the Synergistic Effect of PdAu Catalysts on TiO₂(101) for Robust CO₂ Reduction: A DFT Study. *Appl. Surf. Sci.* **2021**, *563*, 150365. [[CrossRef](#)]
36. Ren, X.; Gao, Y.; Zheng, L.; Wang, Z.; Wang, P.; Zheng, Z.; Liu, Y.; Cheng, H.; Dai, Y.; Huang, B. Oxygen vacancy enhancing CO₂ electrochemical reduction to CO on Ce-doped ZnO catalysts. *Surf. Interfaces* **2021**, *23*, 100923. [[CrossRef](#)]
37. Yui, T.; Kan, A.; Saitoh, C.; Koike, K.; Ibusuki, T.; Ishitani, O. Photochemical Reduction of CO₂ Using TiO₂: Effects of Organic Adsorbates on TiO₂ and Deposition of Pd onto TiO₂. *ACS Appl. Mater. Interfaces* **2011**, *3*, 2594–2600. [[CrossRef](#)]
38. Kreft, S.; Wei, D.; Junge, H.; Beller, M. Recent advances on TiO₂-based photocatalytic CO₂ reduction. *Energy Chem.* **2020**, *2*, 100044. [[CrossRef](#)]
39. Zhou, W.; Guo, J.-K.; Shen, S.; Pan, J.; Tang, J.; Chen, L.; Au, C.-T.; Yin, S.-F. Progress in Photoelectrocatalytic Reduction of Carbon Dioxide. *Acta Phys. Chim. Sin.* **2020**, *36*, 1906048. [[CrossRef](#)]
40. Blochl, P.E. Projector augmented-wave method. *Phys. Rev. B* **1994**, *50*, 17953–17979. [[CrossRef](#)]
41. Kresse, G.; Joubert, D. From ultrasoft pseudopotentials to the projector augmented-wave method. *Phys. Rev. B* **1999**, *59*, 1758–1775. [[CrossRef](#)]
42. Kresse, G.; Hafner, J. Ab-initio molecular-dynamics for open-shell transition-metals. *Phys. Rev. B* **1993**, *48*, 13115–13118. [[CrossRef](#)]
43. Kresse, G. Ab initio molecular dynamics for liquid metals. *J. Non-Cryst. Solids* **1995**, *192–193*, 222–229. [[CrossRef](#)]

44. Kresse, G.; Hafner, J. Ab initio molecular-dynamics simulation of the liquid-metal-amorphous-semiconductor transition in germanium. *Phys. Rev. B* **1994**, *49*, 14251–14269. [[CrossRef](#)]
45. Kresse, G.; Furthmüller, J. Efficiency of ab-initio total energy calculations for metals and semiconductors using a plane-wave basis set. *Comput. Mater. Sci.* **1996**, *6*, 15–50. [[CrossRef](#)]
46. Camellone, M.F.; Fabris, S. Reaction Mechanisms for the CO Oxidation on Au/CeO₂ Catalysts: Activity of Substitutional Au³⁺/Au⁺ Cations and Deactivation of Supported Au⁺ Adatoms. *J. Am. Chem. Soc.* **2009**, *131*, 10473–10483. [[CrossRef](#)]
47. He, Z.; Wen, L.; Wang, D.; Xue, Y.; Lu, Q.; Wu, C.; Chen, J.; Song, S. Photocatalytic Reduction of CO₂ in Aqueous Solution on Surface-Fluorinated Anatase TiO₂ Nanosheets with Exposed {001} Facets. *Energy Fuel* **2014**, *28*, 3982–3993. [[CrossRef](#)]
48. Jónsson, H.; Mills, G.; Jacobsen, K.W. Nudged elastic band method for finding minimum energy paths of transitions. In *Classical and Quantum Dynamics in Condensed Phase Simulations*; Berne, B.J., Ciccotti, G., Coker, D.F., Eds.; World Scientific: Singapore, 1998; p. 385.
49. Henkelman, G.; Uberuaga, B.P.; Jónsson, H. A climbing image nudged elastic band method for finding saddle points and minimum energy paths. *J. Chem. Phys.* **2000**, *113*, 9901–9904. [[CrossRef](#)]
50. Henkelman, G.; Jónsson, H. Improved tangent estimate in the nudged elastic band method for finding minimum energy paths and saddle points. *J. Chem. Phys.* **2000**, *113*, 9978–9985. [[CrossRef](#)]
51. Henkelman, G.; Arnaldsson, A.; Jónsson, H. A fast and robust algorithm for Bader decomposition of charge density. *Comput. Mater. Sci.* **2006**, *36*, 354–360. [[CrossRef](#)]